A Fracture-Mechanics-Based Methodology for Fatigue Life Prediction of Single Crystal Nickel-Based Superalloys

Srikant Ranjan
e-mail: srikant@ufl.edu

Nagaraj K. Arakere[1]
e-mail: nagaraj@ufl.edu

Mechanical and Aerospace Engineering Department,
University of Florida,
Gainesville, FL 32611-6300

A comprehensive fracture-mechanics-based life prediction methodology is presented for fcc single crystal components based on the computation of stress intensity factors (SIFs), and the modeling of the crystallographic fatigue crack growth (FCG) process under mixed-mode loading conditions. The 3D finite element numerical procedure presented for computing SIFs for anisotropic materials under mixed-mode loading is very general and not just specific to fcc single crystals. SIFs for a Brazilian disk specimen are presented for the crack on the {111}) plane in the ⟨101⟩ and ⟨121⟩ directions, which represent the primary and secondary slip directions. Variation of SIFs as a function of thickness is also presented. Modeling of the crystallographic FCG behavior is performed by using the resolved shear stress intensity coefficient, K_{rss}. This parameter is sensitive to the grain orientation and is based on the resolved shear stresses on the slip planes at the crack tip, which is useful in identifying the active crack plane as well as in predicting the crack growth direction. A multiaxial fatigue crack driving force parameter, ΔK_{rss}, was quantified, which can be used to predict the FCG rate and, hence, life in single crystal components subject to mixed-mode fatigue loading. [DOI: 10.1115/1.2838990]

Introduction

Turbine blades in high performance aircraft and rocket engines are increasingly being made of single crystal nickel-based superalloys. Turbine blades and vanes, used in aircraft and rocket engines, are typically the most demanding structural applications for high temperature materials due to the combination of high operating temperature, corrosive environment, high monotonic and cyclic stresses, and long expected component lifetimes, and the enormous consequence of structural failure. Failures of blade components account for 40% of all turbine engine component failures attributable to high cycle fatigue (HCF) [1]. Estimation of blade fatigue life, therefore, represents a very important aspect of durability assessment.

Nickel-based single crystal superalloy materials have a fcc crystal structure, and differ from polycrystalline alloys in that they have orthotropic properties making the position of the crystal lattice relative to the part geometry a significant factor in the overall analysis [2]. The modified Goodman approach currently used for component design does not address important factors that affect HCF, such as crystallographic crack initiation and propagation, magnitude of resolved shear stress amplitudes on slip planes, fretting damage, and interaction with low cycle fatigue (LCF). Rocket engine service presents a different set of requirements that shifts the emphasis to low temperature fatigue and fracture capability, with particular attention given to thermal, cryogenic, and high pressure hydrogen gas exposure [3]. Toward addressing HCF induced component failures, a large body of fatigue test has been collected by the gas turbine and space propulsion industries. However, there currently exists no systematic method for applying this knowledge toward the design of more robust single crystal gas turbine engine components. There is a need to establish a mechanistically based life prediction methodology for fcc single crystal components.

Fatigue failure in PWA1480/1493, a single crystal nickel-based turbine blade superalloy, was investigated by Swanson and Arakere [4] using a combination of experimental LCF fatigue data and 3D finite element (FE) modeling of HPFTP/AT space shuttle main engine (SSME) turbine blades. The maximum shear stress amplitude ($\Delta\tau_{max}$) on the primary slip systems was found to be an effective multiaxial fatigue failure parameter based on the curve fit between $\Delta\tau_{max}$ and cycles to failure. This failure parameter reduces LCF fatigue data obtained with specimens in different crystallographic orientations to an effective *S-N* diagram, with $\Delta\tau_{max}$ as the stress amplitude. This approach is equivalent to a stress-life method used for fatigue design. This procedure was used to evaluate the fatigue life of a SSME turbopump turbine blade using 3D FE analysis (FEA) incorporating elastic anisotropy. Results revealed that a secondary crystallographic orientation had a pronounced effect on fatigue life, leading to the conclusion that control of a secondary orientation has the potential to significantly increase a component's resistance to fatigue crack growth (FCG).

The objectives of this paper are to extend the stress-life approach to the life prediction of single crystal components using the fatigue damage parameter ($\Delta\tau_{max}$), presented by Swanson and Arakere [4], by implementing a fracture mechanics approach to life prediction. This will require computation of stress intensity factors (SIFs) for cracks in fcc single crystals, as a function of crystallographic orientation, under mixed-mode loading conditions, and also modeling of the FCG process. The orientation dependence of material properties for single crystals results in shear coupling and interdependence of (x,y,z) crack tip displacements, leading to mixed-mode loading conditions even when the loading appears to be purely Mode I. Hence, SIF for fcc single crystal materials depends on remote loading, crack size, structural geometry, and crystallographic orientation. In fact, the crystallographic orientation dependence of crack tip displacements, leading to the coupling of KI, KII, and KIII, highlights the difficulty in obtaining generalized SIF solutions for anisotropic and orthotropic materials, and perhaps also explains the dearth of such solutions for practical specimen geometries in published literature. We present

[1]Corresponding author.

Manuscript received October 16, 2006; final manuscript received October 17, 2006; published online March 26, 2008. Review conducted by Dilip R. Ballal.

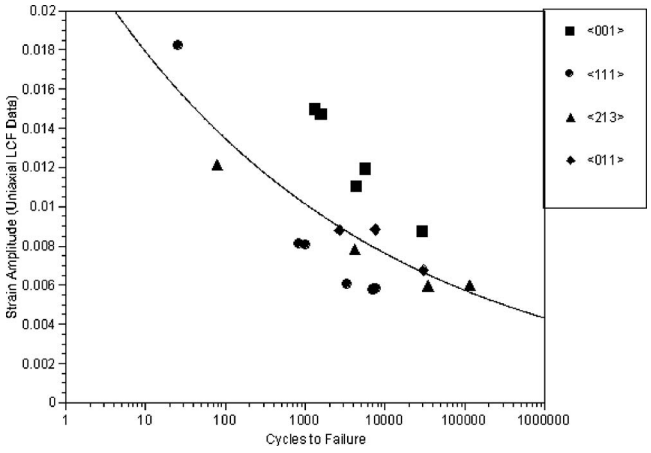

Fig. 1 Strain range versus cycles to failure (N_f) for LCF test data (PWA1493 AT 1200F) [4]

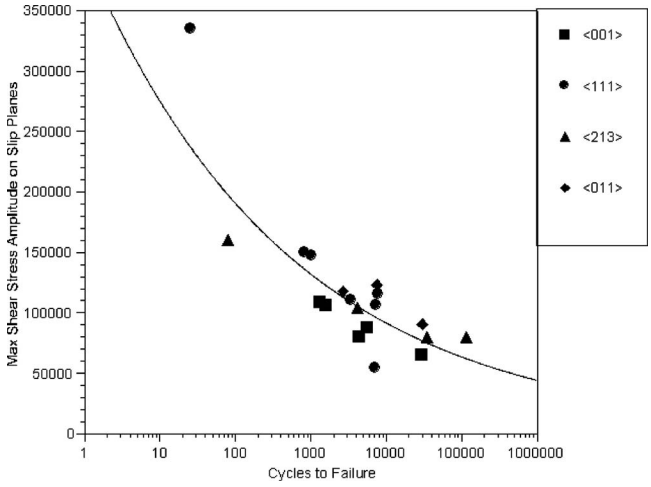

Fig. 2 Shear stress amplitude [$\Delta\tau_{max}$] versus cycles to failure (N_f) [4]

a general numerical procedure for computing SIFs for cracks in fcc single crystals, subject to mixed-mode loading. This represents the first detailed compilation of SIFs for Brazilian disk (BD) specimen as a function of crystallographic orientation. Results are presented for a center-cracked BD specimen, with two specific crystallographic orientations: a (111) crack plane with crack directions $\langle 10\bar{1}\rangle$ and $\langle 12\bar{1}\rangle$. These two crack directions typically represent the fastest and slowest crystallographic crack growth rates, respectively, on the (111) family of octahedral planes of a fcc single crystal and hence, have important implications on estimating FCG life for single crystal components [3]. Even if cracks nucleate on other planes because of local influence from intrinsic defects, such as micropores, carbide particles, and undissolved eutectics, they tend to migrate to the octahedral planes, in the primary slip directions ($\langle 10\bar{1}\rangle$ family of directions), since they represent the paths of least resistance for crack propagation [5]. Results presented show that SIF values are consistently higher for the $\langle 10\bar{1}\rangle$ crack direction, compared to the $\langle 12\bar{1}\rangle$ direction, for identical crack angles and loads [6].

We also present FCG modeling results using a crack driving force parameter based on resolved shear stresses on primary slip planes (ΔK_{rss}). This crack driving force parameter was first highlighted by the experimental work from Telesman and Ghosn [7], which we have adapted in a numerical framework. The ability to compute mixed-mode SIFs and model the FCG process provides tools necessary for establishing a mechanistically based life prediction system. The proposed methodology can be used for computing crystallographic FCG life in single crystal components.

Fatigue Damage Parameter in fcc Single Crystals: Stress-Life Approach for Life

We present a brief description of the fatigue damage parameter, $\Delta\tau_{max}$, developed by Swanson and Arakere [4], for the sake of completeness and also to highlight the differences between the stress-life approach to life prediction and the fracture-mechanics-based life prediction system presented later.

Strain controlled LCF tests conducted at 1200°F in air for PWA1480/1493 uniaxial smooth specimens, for four different orientations are shown in Fig. 1. A wide scatter is observed in the data with poor correlation (R^2=0.469) for a power law fit. The maximum resolved shear stress amplitude ($\Delta\tau_{max}$) on the primary octahedral slip systems for each data point, based on minimum and maximum test strain values and specimen orientation, was calculated based on linear elastic anisotropic assumptions. Figure 2 shows a plot of $\Delta\tau_{max}$ versus cycles to failure. A good correlation (R^2=0.674) is seen for a power law curve fit (Eq. (1)). The plane on which the resolved shear stress reaches a maximum value is also the plane where the critical resolved shear stress (CRSS) is exceeded first, thus making it the dominant slip system to initiate slip or plasticity,

$$\Delta\tau_{max} = 397{,}758N^{-0.1598} \tag{1}$$

We have conducted further experimental and numerical investigations on the evolution of slip in triaxial states of stress and concluded that once slip is initiated on the dominant slip system, if tends to stay on this plane [8]. This sheds further light on why the $\Delta\tau_{max}$ multiaxial fatigue damage parameter collapses the fatigue test data very effectively. The failure planes on the LCF specimens were investigated by Naik et al. [9] and it was found that those planes were indeed the planes where the resolved shear stresses were maximum. The correlation for ($\Delta\tau_{max}$) versus N would be better if some of the high stress data points are corrected for inelastic effects.

Computation of Stress Intensity Factors for fcc Single Crystals Under Mixed-Mode Loading

SIF about a crack tip plays a significant role in the propagation of the crack. The SIF is a measure of intensity near the crack tip under linear elastic conditions. The knowledge of SIF is necessary to predict the growth of a fatigue crack or to determine the residual strength of a cracked structure.

Many methods have been proposed to calculate SIFs for cracks subjected to mixed-mode loading conditions in isotropic elastic solids. Some commonly used methods are J integral [10,11], virtual crack extension [12,13], modified crack closure integral, displacement extrapolation methods [14], etc. None of these proposed methods are able to provide the complete solution for all the three modes (Mode I, II, and III) of SIF for an anisotropic material.

Although a substantial body of literature describes the computation of SIF [11,13,15–29], a generalized numerical solution to calculate SIF for a 3D anisotropic material under a mixed-mode loading condition is unavailable.

It can be shown that mixed-mode SIFs for an anisotropic material can be computed by [6]

$$\begin{Bmatrix} K_{\mathrm{I}} \\ K_{\mathrm{II}} \\ K_{\mathrm{III}} \end{Bmatrix} = [B]^{-1}\{A\}\sqrt{\frac{\pi}{2L_1}} \tag{2}$$

where L_1 is the element length along the crack face (AC=GF) and $\{A\}$ is given as

$$\begin{aligned}\{A\} = {} & 2u_B - u_C + 2u_E - u_F + u_D + \frac{1}{2}\eta(-4u_B + u_C \cdots 4u_E - u_F) \\ & + \frac{1}{2}\eta^2(u_F + u_C - 2u_D)2v_B - v_C + 2v_E - v_F + v_D \\ & + \frac{1}{2}\eta(-4v_B + v_C + \ \ldots \ + 4v_E - v_F) \\ & + \frac{1}{2}\eta^2(v_F + v_C - 2v_D)2w_B - w_C + 2w_E - w_F + w_D \\ & + \frac{1}{2}\eta(-4w_B + w_C + \ \ldots \ + 4w_E - w_F) \\ & + \frac{1}{2}\eta^2(w_F + w_C - 2w_D)\end{aligned} \tag{3}$$

Here u, v, and w are the nodal displacements of nodes B, C, D, E, and F at the crack tip relative to B′, C′, D′, E′, and F′, as shown in Fig. 3.

η is the natural coordinate system value defined as

$$\eta = -\left(\frac{2z}{L_2} + 1\right) \tag{4}$$

L_2 is the length of the element along the crack front (AG=CF) and $[B]^{-1}$ is defined as

$$[B]^{-1} = \begin{bmatrix} \mathrm{Re}\left[\frac{i}{\mu_1 - \mu_2}(q_2 - q_1)\right]\frac{1}{D} & \mathrm{Re}\left[\frac{-i}{\mu_1 - \mu_2}(p_2 - p_1)\right]\frac{1}{D} & 0 \\ \mathrm{Re}\left[\frac{-i}{\mu_1 - \mu_2}(\mu_1 q_2 - \mu_2 q_1)\right]\frac{1}{D} & \mathrm{Re}\left[\frac{i}{\mu_1 - \mu_2}(\mu_1 p_2 - \mu_2 p_1)\right]\frac{1}{D} & 0 \\ 0 & 0 & \frac{1}{\sqrt{c_{44}c_{55} - c_{45}^2}} \end{bmatrix} \tag{5}$$

As is apparent from the $[B]^{-1}$ matrix, the K_{I} and K_{II} are the only coupled SIFs (functions of u and v) and the K_{III} is a function of w only.

D is the determinant of the equation

$$D = \begin{vmatrix} \mathrm{Re}\left[\frac{i}{\mu_1 - \mu_2}(\mu_1 p_2 - \mu_2 p_1)\right] & \mathrm{Re}\left[\frac{i}{\mu_1 - \mu_2}(p_2 - p_1)\right] \\ \mathrm{Re}\left[\frac{i}{\mu_1 - \mu_2}(\mu_1 q_2 - \mu_2 q_1)\right] & \mathrm{Re}\left[\frac{i}{\mu_1 - \mu_2}(q_2 - q_1)\right] \end{vmatrix} \tag{6}$$

μ_1 and μ_2 are the roots of the fourth order characteristic equation

$$a_{11}\mu^4 - 2a_{16}\mu^3 + (2a_{12} + a_{66})\mu^2 - 2a_{26}\mu + a_{22} = 0 \tag{7}$$

and are given by

$$\mu_j = \alpha_j + i\beta_j \text{ and } \beta_j > 0$$

(as μ_j can only be a complex number [30] (for the details, refer to Ranjan [6]),

$$p_j = a_{11}\mu_j^2 + a_{12} - a_{16}\mu_j$$

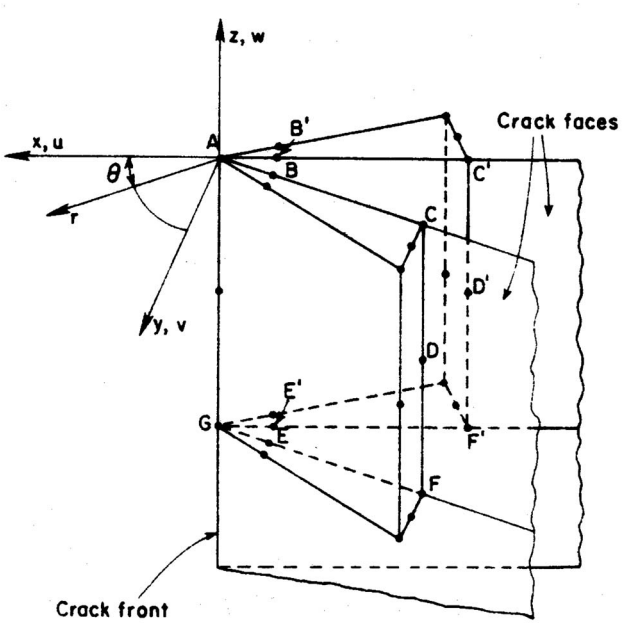

Fig. 3 Arrangement of quarter-point wedge elements along segment of crack front with nodal lettering convention [31]

$$q_j = a_{12}\mu_j + \frac{a_{22}}{\mu_j} - a_{26} \tag{8}$$

For plane stress,

$$a_{11} = \frac{1}{E_{11}}, \quad a_{22} = \frac{1}{E_{22}}, \quad a_{21} = a_{12} = -\frac{\nu_{12}}{E_{11}}, \quad a_{66} = \frac{1}{G_{12}} \tag{9}$$

For plane strain,

$$a_{ij} = a_{ij} - \frac{a_{i3}a_{j3}}{a_{33}} \tag{10}$$

Equation (2) is used to calculate the SIF at the crack tip by the displacement method, which is one of the most commonly used methods to get the value accurately. The FE method was used to calculate the displacements at the crack tip. The commercial software ANSYS was used for FEA modeling. The crack tip nodal displacements were then extracted from the FEA model and fed to the analytical equations explained above to calculate all the three modes of SIFs.

Single Crystal Specimen Geometries Used for Mixed-Mode Loading

The specimen modeled was a circular BD specimen, loaded in compression. Details of the BD specimen analyzed are given in Table 1. This specimen with center crack has a mode mixity at the crack tip, which varies as function of the crack angle ϕ, shown in Fig. 4. The crack lies on the {111} plane, and the crack directions used are the ⟨101⟩ and ⟨121⟩ families of directions. These specimen and crack orientations have been checked very carefully based on experimentally observed FCG rates (FCGRs) [32].

Table 1 Geometrical and material properties of the BD specimen analyzed

E	106.2 GPa	G	108.2 GPa	ν	0.4009
W	2.794 cm	$2a/W$	0.2–0.8	t	0.254 cm
F	4.448 kN				

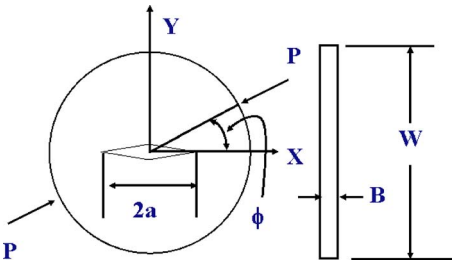

Fig. 4 BD specimen with center crack lying in the (111) plane and oriented along the $[10\bar{1}]$ direction

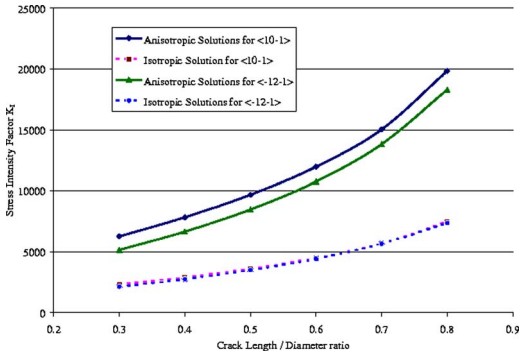

Fig. 6 K_I versus $2a/W$ ratio for $[10\bar{1}]$ and $[\bar{1}2\bar{1}]$ orientations of BD specimen at $\phi=0$ deg

Figure 5 shows that the crack plane lies on the (111) plane and is directed along the $\langle\bar{1}2\bar{1}\rangle$ direction. This slip system has been explained with the help of octahedral slip planes (Fig. 5, right side).

SIF Results. From the BD specimen results (Figs. 6–11), it can be seen that the magnitude of SIF for the $[10\bar{1}]$ orientation is always greater than the corresponding values of the $[\bar{1}2\bar{1}]$ orientation, thus enabling a crack to propagate faster on the $[10\bar{1}]$ plane than on the $[\bar{1}2\bar{1}]$ plane under identical fatigue loading. For the $[10\bar{1}]$ orientation, the crack closure angle is ~18 deg, whereas it is ~30 deg for the $[\bar{1}2\bar{1}]$ orientation (Fig. 9).

Following the work of Saouma and Sikiotis [31], the calculated values for K_{III} were found to be negligible. The discrepancies were found in the formulation of Eq. (5), and we believe that the form of Eq. (5), shown in this paper is appropriate to use in fcc single crystals, as it correctly gives rise to all the three modes of SIFs. As a result of the coupling of displacements at the crack tip due to anisotropy, non-negligible values of K_{III} were found, and they varied with respect to the applied force, crack length, and crack angle.

The BD specimen SIFs were further analyzed along the thickness for the $[10\bar{1}]$ and $[\bar{1}2\bar{1}]$ crack orientations due to change in crack length and crack angle. They were calculated at five different points along the thickness at the crack front, as shown in Fig. 12. A plane stress assumption was made at the surface of the BD specimen (Planes 1 and 5), and a plane strain assumption was made at all the interior points (Planes 2–4).

In order to check the difference in SIF of isotropic BD specimen and orthotropic BD specimen with change in load angle and with crack, under similar loading condition and specimen geometry, two models were analyzed. Due to the limitation of space, this analysis could not be presented here, but can be found in Ranjan [6].

From Figs. 13 and 15, it can be seen that the crack closure angle (where K_I is almost zero) was reached at ~18 deg for the $[10\bar{1}]$ orientation, whereas it was ~30 deg for the $[\bar{1}2\bar{1}]$ orientation, as was observed in Fig. 9. K_I can be seen as symmetric for the $[\bar{1}2\bar{1}]$ orientation across the thickness, whereas it is not for the $[10\bar{1}]$ orientation. In general, K_I inside the surface (Planes 2, 3, and 4, Fig. 12) than those at the crack edges (Planes 1 and 5, Fig. 12).

The absolute value of K_{II} becomes maximum at an angle of ~24 deg for the $[10\bar{1}]$ orientation, whereas for the $[\bar{1}2\bar{1}]$ orientation, it is ~36 deg (Figs. 14 and 16), as also illustrated in Fig. 10. It is interesting to observe that SIFs (Figs. 15–18) (K_I, K_{II}, and K_{III}) are symmetric about the midplane for the $[\bar{1}2\bar{1}]$ orientation. This is due to the symmetry observed more only for the crack lying along the $\langle 121\rangle$ direction than for that lying along the $\langle 101\rangle$ direction on the {111} plane, as shown in Fig. 19.

K_{III} is maximum at an angle of ~48 deg for the $[\bar{1}2\bar{1}]$ orientated BD specimen, as can be clearly seen in Fig. 11. The values of K_{III} (Fig. 17) for the $[10\bar{1}]$ orientation at one of the faces (Plane 1, thickness=0) are always greater than those at the other face (Plane 5, thickness=1), and reach maximum at an angle of 30–36 deg. The maximum value of K_{III} shown in Fig. 11 is at ~25 deg because the values were calculated at an offset to the midplane, which can be verified from the offset value taken from Fig. 17.

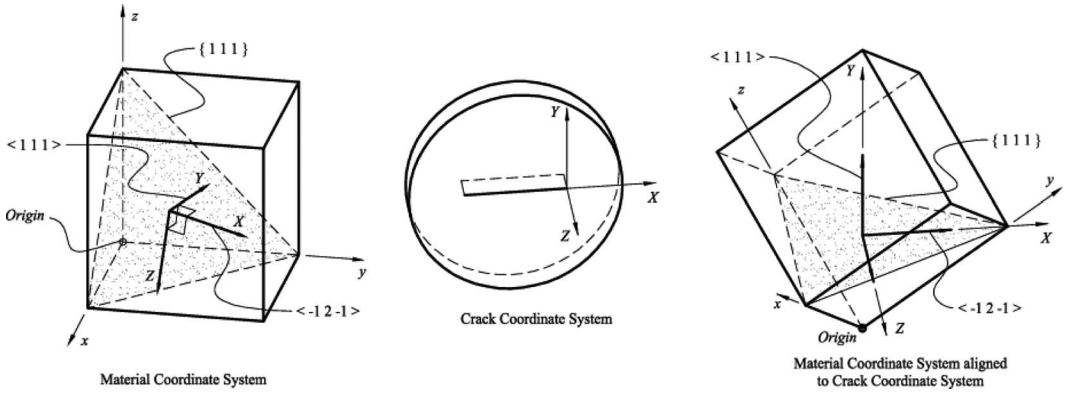

Fig. 5 BD specimen having center crack lying in the {111} slip plane and aligned along the $[\bar{1}2\bar{1}]$ direction

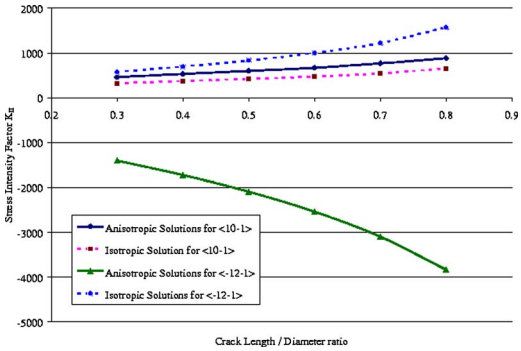

Fig. 7 K_{II} versus $2a/W$ ratio for $[10\bar{1}]$ and $[\bar{1}2\bar{1}]$ orientations of BD specimen at $\phi=0$ deg

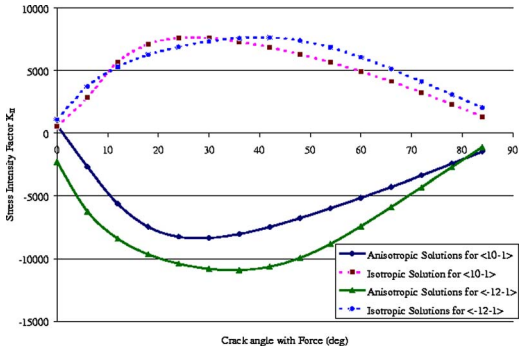

Fig. 10 K_{II} versus crack angle with force for $[10\bar{1}]$ and $[\bar{1}2\bar{1}]$ orientations of BD specimen at $2a/W=0.55$

For the $[\bar{1}2\bar{1}]$ orientation (Figs. 15–18), it can be seen that K_I, K_{II}, and K_{III} are always symmetric across the thickness (because of the symmetry about the midplane, as shown in Fig. 19). At the midplane, K_{III} is always zero, which means that there is no out of plane displacement at the midplane.

Using the above analysis, we can find the profile of the crack growth inside a specimen, which can be crucial for the life assessment of an anisotropic material.

Crystallographic Fatigue Crack Growth

Several studies have been conducted on FCG of Ni-based single crystals [33–37], and all of these studies have shown that FCG is highly sensitive to the orientation of the crystal and that the crack plane is crystallographic and follows a single slip plane or a combination of slip planes. Since shear decohesion on a slip plane is caused by dislocation motion, many researchers have suggested that the resolved shear stress acting on the active slip plane ahead of a crack tip must be responsible for the propagation of the fatigue crack [35,38,39]. The dislocation motion is controlled by the forces at the crack tip, which is directly related to the resolved shear stress on the slip plane. Therefore, the rate of shear decohesion must be related to the "resolved shear stress intensity" (RSSI) at the crack tip. The active shear decohesion plane or planes must be the slip plane(s) with a high RSSI. If the RSSI on a plane is much higher than all the other slip planes, then the plane must be the primary plane for shear decohesion and the slip plane becomes the crack plane. However, if the resolved shear stresses on two or more of the slip systems are comparable, then the shear decohesion will take place on all of those slip planes and the macrocrack

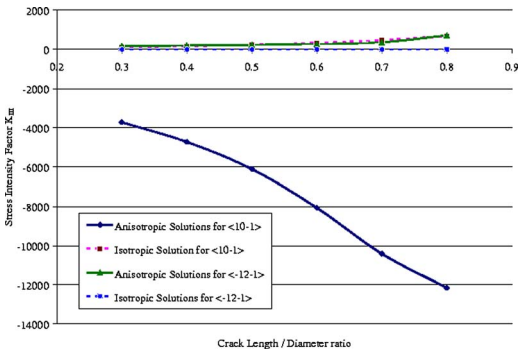

Fig. 8 K_{III} versus $2a/W$ ratio for $[10\bar{1}]$ and $[\bar{1}2\bar{1}]$ orientations of BD specimen at $\phi=0$ deg

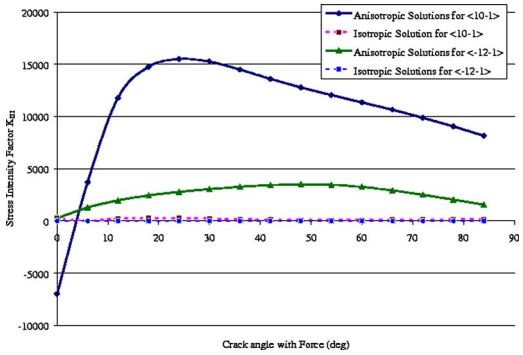

Fig. 11 K_{III} versus crack angle with force for $[10\bar{1}]$ and $[\bar{1}2\bar{1}]$ orientations of BD specimen at $2a/W=0.55$

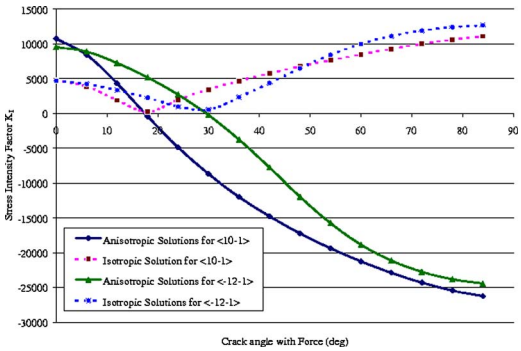

Fig. 9 K_I versus crack angle with force for $[10\bar{1}]$ and $[\bar{1}2\bar{1}]$ orientations of BD specimen at $2a/W=0.55$

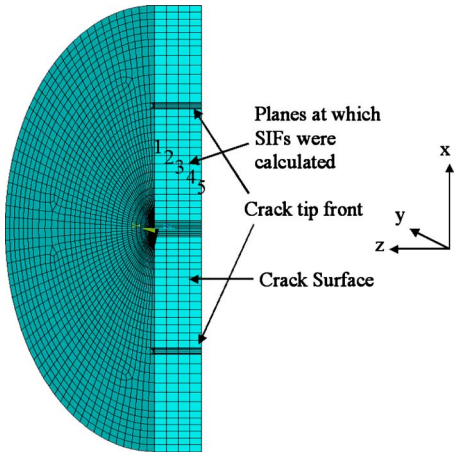

Fig. 12 Half meshed model of BD specimen and the crack coordinate system

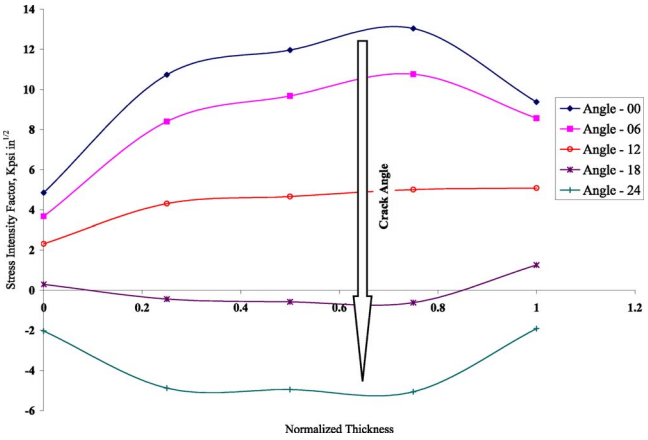

Fig. 13 Variation of SIF K_I along BD specimen thickness at different crack angle for the $[10\bar{1}]$ orientation

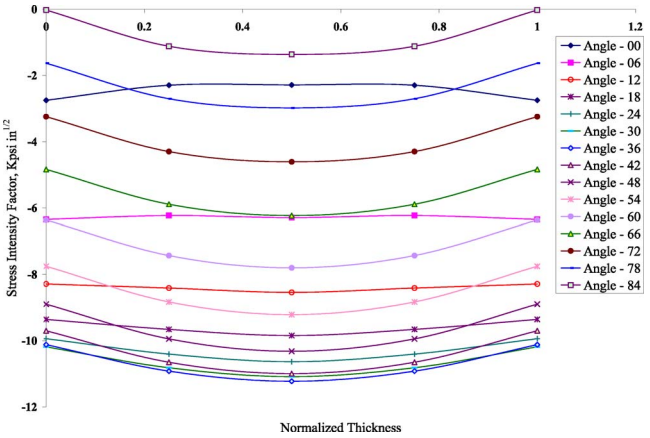

Fig. 16 Variation of SIF K_{II} along BD specimen thickness at different crack angle for the $[\bar{1}2\bar{1}]$ orientation

plane will not follow a single slip plane; this was shown by Telesman and Ghosn [7]. Even though macroscopic crack was observed along the (001) plane inclined 7 deg to the starter notch, the microscopic slip was observed on the (111) slip planes, inclined 52 deg and −38 deg to the starter notch.

If a crack surface is a slip plane, it is logical that the crack growth rate on that slip plane will correlate with its RSSI.

Chen and Liu [40] proposed a crack driving force parameter for correlating FCG data, which is based on the resolved shear stresses on the active slip plane(s). This parameter may be better than ΔK for the correlation of FCG data since it takes into consideration the deformation mechanisms, grain orientation, and actual crack path.

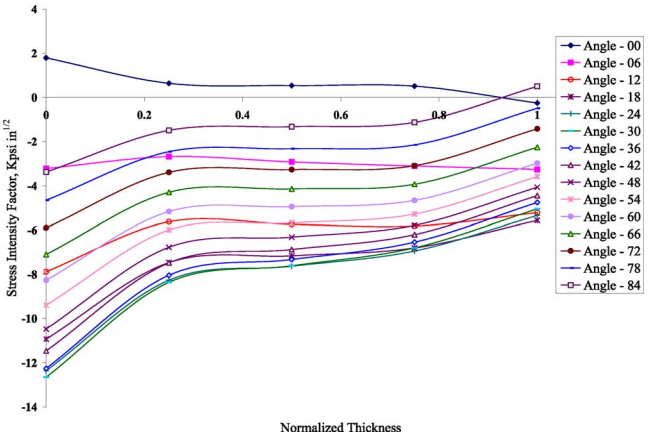

Fig. 14 Variation of SIF K_{II} along BD specimen thickness at different crack angle for the $[10\bar{1}]$ orientation

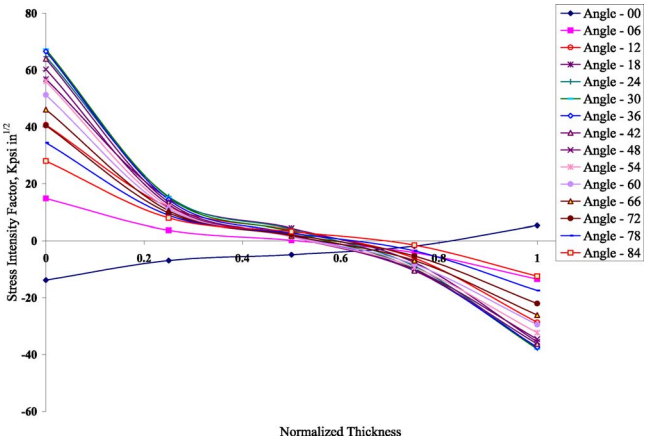

Fig. 17 Variation of SIF K_{III} along BD specimen thickness at different crack angle for the $[10\bar{1}]$ orientation

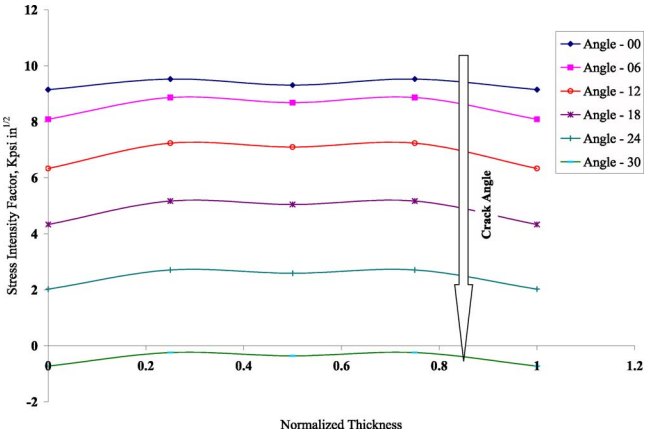

Fig. 15 Variation of SIF K_I along BD specimen thickness at different crack angle for the $[\bar{1}2\bar{1}]$ orientation

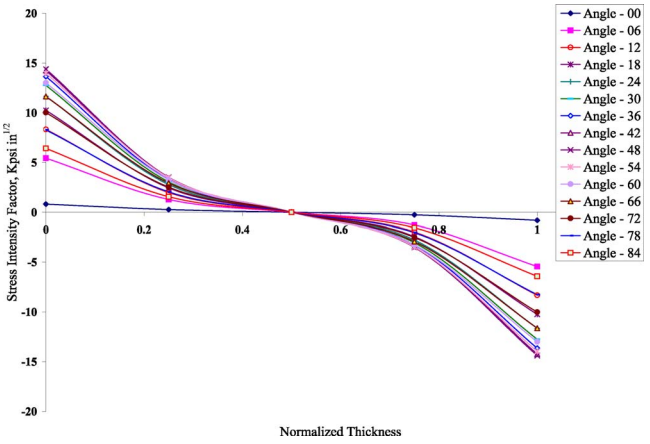

Fig. 18 Variation of SIF K_{III} along BD specimen thickness at different crack angle for the $[\bar{1}2\bar{1}]$ orientation

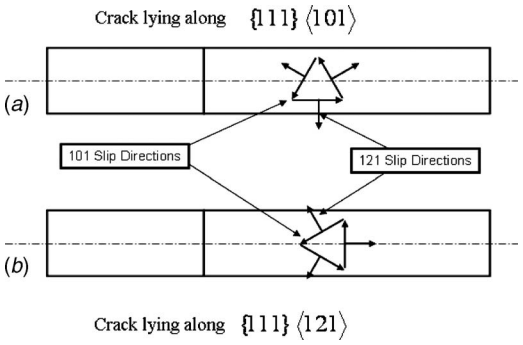

Fig. 19 (*a*) Unsymmetry about midplane for crack oriented along {111} ⟨101⟩; (*b*) symmetry for crack lying along {111} ⟨121⟩

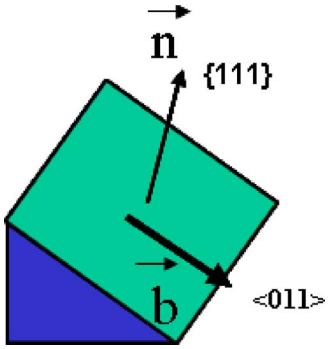

Fig. 21 Burgers vector b is along slip direction ⟨011⟩ and slip plane direction is normal vector n along ⟨111⟩

The resolved shear stress field of a slip system is defined by its intensity coefficient, which can be calculated once Modes I, II, and III crack tip fields are obtained.

The resolved shear stress is given by [41]

$$\tau_{\text{rss}} = \frac{1}{b} b_i \sigma_{ij} n_j \tag{11}$$

where b_i and b are the Burgers vector and its magnitude, n_j is the unit normal vector of the slip plane, and σ_{ij} is the crack tip stress tensor field given by [40]

$$[\sigma_{ij}] = \frac{1}{\sqrt{2\pi r}}[K_{\text{I}} f_{ij}^{\text{I}}(\theta) + K_{\text{II}} f_{ij}^{\text{II}}(\theta) + K_{\text{III}} f_{ij}^{\text{III}}(\theta)] \tag{12}$$

where r and θ are the local polar coordinates at the crack tip, as shown in Fig. 20; $f_{ij}(\theta)$ are the angular component of the stress field. Substituting Eq. (12) into Eq. (11), the resolved shear stress is

$$\tau_{\text{rss}} = \frac{1}{\sqrt{2\pi r}}[b_i^n][K_{\text{I}} f_{ij}^{\text{I}}(\theta) + K_{\text{II}} f_{ij}^{\text{II}}(\theta) + K_{\text{III}} f_{ij}^{\text{III}}(\theta)][n_j] \tag{13}$$

where b_i^n and n_j are the unit Burgers vectors and unit normal vectors of the slip planes, respectively.

The above equation indicates that τ_{rss} preserves the $1/\sqrt{r}$ singularity, and the intensity of τ_{rss} is dependent on the crystal orientation relative to the crack surface. For a given crystal orientation and crack geometry, the angle θ is equal to the angle between the trace of a particular slip plane on the plane normal to the slip plane and the horizontal axis. The intensity of τ_{rss} is linearly proportional to the quantity RSSI coefficient K_{rss}, which for a given slip system can be defined as the limiting value of the resolved shear stress τ_{rss} multiplied by $\sqrt{2\pi r}$ as r approaches zero [7,40]

$$K_{\text{rss}} = \lim_{r \to 0} \tau_{\text{rss}} \sqrt{2\pi r} \tag{14}$$

where r is the distance of the crack tip and τ_{rss} is defined as the projection of the stress tensor $[\sigma]$ on a plane whose outward normal is **n** in the direction of slip **b** (Fig. 21). The two distinct advantages in using K_{rss} are as follows: (1) The dependency of τ_{rss} on r is eliminated; (2) the angle θ has a definite physical meaning, which is directly related to the orientation of the slip system.

The state of stress on a slip plane, under mixed-mode loading, whose trace on a plane normal to crack plane makes an angle θ with the horizontal axis (Figs. 20 and 22), can be defined as [6]

$$\begin{Bmatrix} \sigma_x \\ \sigma_y \\ \sigma_z \\ \tau_{yz} \\ \tau_{zx} \\ \tau_{xy} \end{Bmatrix} = \frac{1}{\sqrt{2\pi r}} \begin{bmatrix} d_{11} & d_{12} & 0 \\ d_{21} & d_{22} & 0 \\ d_{31} & d_{32} & d_{33} \\ 0 & 0 & d_{43} \\ 0 & 0 & d_{53} \\ d_{61} & d_{62} & 0 \end{bmatrix} \cdot \begin{Bmatrix} K_{\text{I}} \\ K_{\text{II}} \\ K_{\text{III}} \end{Bmatrix} \tag{15}$$

where

$$d_{11} = \text{Re}\left[\frac{\mu_1\mu_2}{\mu_1 - \mu_2}\left(\frac{\mu_2}{b_2} - \frac{\mu_1}{b_1}\right)\right], \quad d_{12} = \text{Re}\left[\frac{1}{\mu_1 - \mu_2}\left(\frac{\mu_2^2}{b_2} - \frac{\mu_1^2}{b_1}\right)\right]$$

$$d_{21} = \text{Re}\left[\frac{1}{\mu_1 - \mu_2}\left(\frac{\mu_1}{b_2} - \frac{\mu_2}{b_1}\right)\right], \quad d_{22} = \text{Re}\left[\frac{1}{\mu_1 - \mu_2}\left(\frac{1}{b_2} - \frac{1}{b_1}\right)\right]$$

$$d_{3j} = \begin{cases} 0 & \text{plane stress} \\ -\dfrac{d_{1j}a_{13} + d_{2j}a_{23} + d_{6j}a_{36}}{a_{33}} & \text{plane strain} \end{cases} \qquad j = 1,2$$

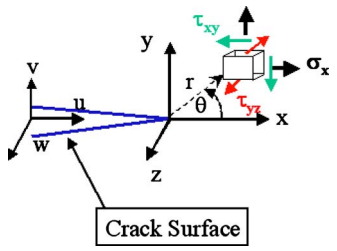

Fig. 20 Details of crack tip displacements and stresses at a distance r and θ from the crack tip in the crack coordinate system

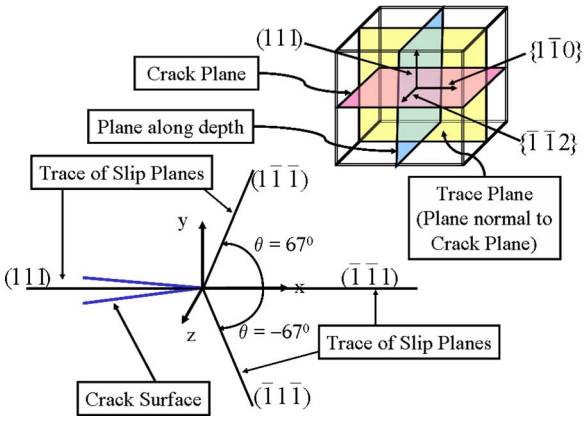

Fig. 22 Trace of primary slip planes on the plane normal to the crack plane

Table 2 The geometry and loading condition of the three BD specimens tested [43].

Specimen	orientation	Test temperature (°C)	Test frequency (Hz)	Load ratio R
A	(111) ⟨110⟩	23	40	0.1
B	(111) ⟨110⟩	23	10	0.1
C	(111) ⟨110⟩	23	10	0.1

Specimen	Diameter W (mm)	Thickness t (mm)	Initial crack length a (mm)	Crack angle with load θ (deg)
A	28.00	2.12	4.16	27.27
B	27.97	2.23	4.16	16
C	28.03	2.20	2.27	16

$$d_{33} = \begin{cases} 0 & \text{plane stress} \\ -\dfrac{d_{43}a_{34} + d_{53}a_{35}}{a_{33}} & \text{plane strain} \end{cases}$$

$$d_{43} = \mathrm{Re}\left[\frac{1}{b_3}\right], \quad d_{61} = \mathrm{Re}\left[\frac{\mu_1\mu_2}{\mu_1 - \mu_2}\left(\frac{1}{b_1} - \frac{1}{b_2}\right)\right]$$

$$d_{53} = -\mathrm{Re}\left[\frac{\mu_3}{b_3}\right], \quad d_{62} = \mathrm{Re}\left[\frac{1}{\mu_1 - \mu_2}\left(\frac{\mu_1}{b1} - \frac{\mu_2}{b2}\right)\right]$$

$$b_i = \sqrt{\cos(\theta) + \mu_i \sin(\theta)}, \quad i = 1,2,3$$

μ_1 and μ_2 are the two roots with positive imaginary parts as defined by the equation

$$a_{11}\mu^4 - 2a_{16}\mu^3 + (2a_{12} + a_{66})\mu^2 - 2a_{26}\mu + a_{22} = 0 \qquad (16)$$

and μ_3 is the root of the characteristic equation [42]

$$a_{55}\mu^2 - 2a_{45}\mu + a_{44} = 0 \qquad (17)$$

It should be noted that the compliance constants ($a_{i,3}(i = 1,2,\ldots,6)$) used for the expression ($d_{3,j}(j=1,2,3)$) are the ones as given by Eq. (9).

The above equations, when used in conjunction with Eqs. (11) and (14), give K_{rss} on all the 12 slip systems for a fcc single crystal superalloy,

$$K_{rss} = [b_i^n][n_j]\begin{bmatrix} d_{11} & d_{12} & 0 \\ d_{21} & d_{22} & 0 \\ d_{31} & d_{32} & d_{33} \\ 0 & 0 & d_{43} \\ 0 & 0 & d_{53} \\ d_{61} & d_{62} & 0 \end{bmatrix} \cdot \begin{Bmatrix} K_{\mathrm{I}} \\ K_{\mathrm{II}} \\ K_{\mathrm{III}} \end{Bmatrix} \qquad (18)$$

Three BD specimen of a PWA1422 single crystal material were tested (Table 2) to correlate the FCG data with the calculated ΔK_{rss}.

The mixed-mode SIFs were calculated for all the three specimens on the midplane of the BD specimens, based on plane strain assumption. K_{rss} was calculated using Eq. (14), where the state of stress obtained from Eq. (15) was multiplied by Schmid's factor for fcc single crystal (refer to Ranjan [6]) to get the RSS on all the 12 primary slip systems. The traces of the two slip planes $(\bar{1}1\bar{1})$ and $(1\bar{1}\bar{1})$ were found to make equal angles with the (111) plane (67.78 deg), while the trace of the plane $(\bar{1}\bar{1}1)$ was found to make 0 deg with the crack plane (111), as shown in Fig. 22.

The load ratio R (minimum load/maximum load) was 0.1 (Table 2), as the load on the BD specimen was always tensile. As SIFs are linearly proportional to the load applied, K_{rss} was multiplied with R to get the ΔK_{rss}.

The maximum K_{rss} was found to be on the (111) slip plane for all the three specimens (first row of Tables 3–5), as observed in the experiment test results (Fig. 23). The calculated ΔK_{rss} was plotted against da/dN on a log-log scale to check the validity of the model (Fig. 24). After ΔK_{rss} reaches 10 MPa $\sqrt{\mathrm{m}}$, a linear plot can be seen, which might correspond to Region II (Paris region) where the crack growth rate is directly proportional to the applied ΔK on a log-log basis. However, not enough data are available to support the theory. However, below a ΔK_{rss} of 8 MPa $\sqrt{\mathrm{m}}$, an accelerated crack growth can be seen between 5 MPa $\sqrt{\mathrm{m}}$ and 7 MPa $\sqrt{\mathrm{m}}$, in the threshold region, region or Stage I. The lines drawn through those points yield ΔK_{th} on the ΔK_{rss} axis, which is called fatigue threshold SIF. The average ΔK_{th} of the three speci-

Table 3 K_{rss} for 12 primary slip systems with increasing crack length for specimen *A*

Slip plane	Slip direction	K_{rss} in MPa $\sqrt{m}$ for Specimen *A* with increasing crack length a in mm: 5.25	5.36	5.66	5.82	6.09	6.10	6.12
(111)	$[10\bar{1}]$	−6.45	−6.59	−6.59	−7.18	−7.58	−7.61	−7.64
(111)	$[0\bar{1}1]$	1.91	1.97	2.13	2.22	2.40	2.42	2.43
(111)	$[1\bar{1}0]$	−4.54	−4.63	−4.83	−4.96	−5.18	−5.19	−5.21
$(\bar{1}1\bar{1})$	$[10\bar{1}]$	−1.17	−1.18	−1.21	−1.23	−1.27	−1.27	−1.27
$(\bar{1}1\bar{1})$	[110]	1.00	0.99	0.95	0.92	0.85	0.85	0.85
$(\bar{1}1\bar{1})$	[011]	2.17	2.17	2.16	2.16	2.12	2.12	2.12
$(1\bar{1}\bar{1})$	[110]	0.83	0.87	0.98	1.05	1.18	1.18	1.19
$(1\bar{1}\bar{1})$	$[0\bar{1}1]$	3.07	3.09	3.10	3.12	3.11	3.11	3.11
$(1\bar{1}\bar{1})$	[101]	3.90	3.96	4.08	4.16	4.28	4.29	4.30
$(\bar{1}\bar{1}1)$	[011]	1.91	1.97	2.13	2.22	2.40	2.42	2.43
$(\bar{1}\bar{1}1)$	[101]	−2.99	−3.02	−3.08	−3.11	−3.15	−3.15	−3.16
$(\bar{1}\bar{1}1)$	$[1\bar{1}0]$	−4.91	−4.99	−5.20	−5.33	−5.55	−5.57	−5.59

Table 4 K_{rss} for 12 primary slip systems with increasing crack length for specimen *B*

Slip plane	Slip direction	K_{rss} in MPa $\sqrt{m}$ for Specimen *B* with increasing crack length *a* in mm						
		8.06	8.38	8.67	9.09	9.46	9.87	10.13
(111)	$[10\bar{1}]$	−6.11	−5.95	−6.20	−6.39	−6.56	−6.75	−6.91
(111)	$[0\bar{1}1]$	1.03	1.12	1.29	1.51	1.71	1.93	2.10
(111)	$[1\bar{1}0]$	−5.08	−4.83	−4.91	−4.88	−4.85	−4.81	−4.81
$(\bar{1}1\bar{1})$	$[10\bar{1}]$	−1.61	−1.48	−1.46	−1.39	−1.33	−1.25	−1.21
$(\bar{1}1\bar{1})$	[110]	2.59	2.29	2.14	1.84	1.56	1.23	1.02
$(\bar{1}1\bar{1})$	[011]	4.20	3.77	3.60	3.23	2.89	2.49	2.22
$(1\bar{1}\bar{1})$	[110]	−0.17	−0.02	0.13	0.36	0.56	0.79	0.96
$(1\bar{1}\bar{1})$	$[0\bar{1}1]$	5.42	4.90	4.73	4.31	3.92	3.47	3.17
$(1\bar{1}\bar{1})$	[101]	5.25	4.89	4.86	4.67	4.48	4.26	4.13
$(\bar{1}\bar{1}1)$	[011]	1.03	1.12	1.29	1.51	1.71	1.93	2.10
$(\bar{1}\bar{1}1)$	[101]	−4.66	−4.25	−4.15	−3.86	−3.60	−3.29	−3.10
$(\bar{1}\bar{1}1)$	$[1\bar{1}0]$	−5.68	−5.37	−5.44	−5.37	−5.30	−5.22	−5.19

mens has been taken (~4.3 MPa $\sqrt{m}$) at a given load ratio R(=0.1). Below this value ($\Delta K_{rss} < \Delta K_{th}$) either crack growth does not occur by cyclic loading, i.e., $da/dN=0$ and the specimen can have infinite life, or it grows at undetectable rates. The value of ΔK_{th} can be affected by alterations in the material microstructure, load ratio, environment, and crack size [44]. However, the cyclic SIF (ΔK_{rss}) is not the only load parameter to control the FCG rate because da/dN, at a given ΔK_{rss}, can increase with the increase in load ratio R as

$$K_{max} = \frac{\Delta K_{rss}}{(1-R)}$$

The advantage of ΔK_{rss} lies in the ability to predict the actual microscopic fatigue fracture mechanisms, and it also takes into consideration the orientation of the grain. The ΔK_{rss} is also a multiaxial fatigue stress parameter, incorporating resolved shear stress on primary slip systems.

Conclusions

The results obtained can be summarized as follows:

1. An analytical method was developed for the calculation of all three modes of SIFs as a function of crystallographic orientation for an orthotropic material, which can be applied to any anisotropic material if all the material constants are known.
2. Mode *I* (K_I) was always found to be greater for $[10\bar{1}]$ than for the $[\bar{1}2\bar{1}]$ orientation. For an orthotropic material, K_I was

Table 5 K_{rss} for 12 primary slip systems with increasing crack length for specimen *C*

Slip plane	Slip direction	K_{rss} in MPa $\sqrt{m}$ for Specimen *C* with increasing crack length *a* in mm						
		7.74	8.31	8.78	9.02	9.79	10.93	11.55
(111)	$[10\bar{1}]$	−12.42	−14.40	−16.41	−17.54	−21.82	−30.65	−37.37
(111)	$[0\bar{1}1]$	1.82	2.62	3.50	4.02	6.10	10.75	14.46
(111)	$[1\bar{1}0]$	−10.60	−11.78	−12.91	−13.52	−15.72	−19.91	−22.91
$(\bar{1}1\bar{1})$	$[10\bar{1}]$	−3.45	−3.65	−3.82	−3.90	−4.14	−4.41	−4.48
$(\bar{1}1\bar{1})$	[110]	5.80	5.74	5.50	5.32	4.34	1.53	−0.86
$(\bar{1}1\bar{1})$	[011]	9.24	9.39	9.32	9.22	8.48	5.94	3.62
$(1\bar{1}\bar{1})$	[110]	−0.68	−0.16	−0.46	−0.83	−2.38	6.02	9.01
$(1\bar{1}\bar{1})$	$[0\bar{1}1]$	11.85	12.18	12.27	12.24	11.73	9.48	7.33
$(1\bar{1}\bar{1})$	[101]	11.17	12.02	12.72	13.07	14.11	15.50	16.33
$(\bar{1}\bar{1}1)$	[011]	1.82	2.62	3.50	4.02	6.10	10.75	14.46
$(\bar{1}\bar{1}1)$	[101]	−10.09	−10.52	−10.78	−10.88	−10.99	−10.37	−9.50
$(\bar{1}\bar{1}1)$	$[1\bar{1}0]$	−11.91	−13.14	−14.29	−14.90	−17.09	−21.12	−23.96

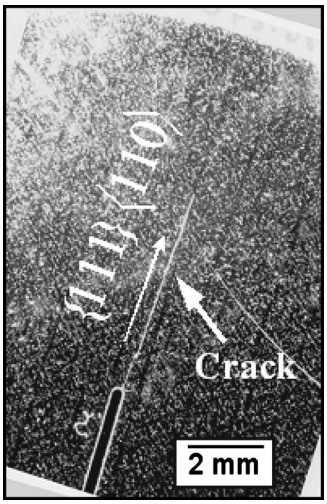

Fig. 23 Crack growth on the {111} slip plane can be observed for BD specimen *B* [43]

found to be nonzero at the crack closure due to the coupling of the nodal displacements, whereas for an isotropic material, it was zero.

3. The magnitude of K_{II} for $[\bar{1}2\bar{1}]$ was always found to be greater than that for the $[10\bar{1}]$ orientation, but the difference was not much.
4. Mode III SIF (K_{III}) existed because of the coupling of displacements at the crack tip due to anisotropy. K_{III} for $[10\bar{1}]$ was found to be much bigger than that for the $[\bar{1}2\bar{1}]$ orientation for the BD specimen. This plays an important role in the calculation of effective K to predict the life of an anisotropic material.
5. SIFs calculated for the $[\bar{1}2\bar{1}]$ crack orientation was found to be symmetric, which was due to the symmetry of $\langle 121\rangle$ about the midplane, as shown in Fig. 19, whereas due to the unsymmetrical nature of the $\langle 101\rangle$ orientation, the calculated SIFs varied along the thickness for the $[10\bar{1}]$ crack orientation. This variation can very well be used to predict the crack growth profile across the thickness.
6. The crack closure for the $[10\bar{1}]$ orientation was found to be 18 deg, whereas it was 30 deg for the $[\bar{1}2\bar{1}]$ orientation for the BD specimen, which shows the importance of knowledge of secondary orientation.
7. As shear decohesion is caused by dislocation motion, it was expected that the orientation of the crack plane must be related to the active slip plane(s). The fatigue damage parameter K_{rss} was calculated for all the 12 primary slip systems and for all the three BD specimens. The $K_{rss,max}$ was found on the {111} plane, which also happened to be the crack growth plane for all the three BD specimens. Therefore, for a single active slip plane, the maximum resolved shear stress provides the primary driving force for dislocation motion, the shear decohesion process leading to the crack growth process.
8. The parameter K_{rss} is well suited in identifying the active crack plane, as well as in predicting the microscopic crack growth direction. It is also an effective multiaxial crack driving force parameter.
9. The method developed is not related to any specific geometry. Therefore, it can be used for any kind of geometry and for any general anisotropic material to calculate mixed-mode SIFs at the crack tip. Therefore, crack growth rate and, hence, life of any material can be predicted.

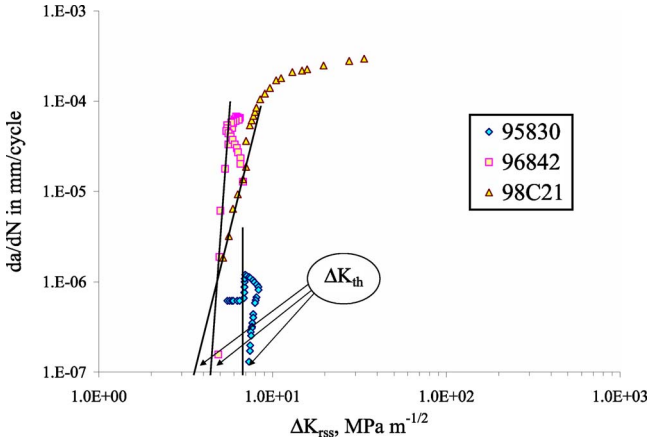

Fig. 24 FCG rate of three specimens *A*, *B*, and *C* as a function of ΔK_{rss}

However, additional experimental data are required to study FCG on the {111} family of planes for the $\langle 101\rangle$ family of crack directions. More experimental data are needed in Region II to get the accurate result to predict lifing. Also, experimental data for crack plane orientations other than slip planes, e.g., $\langle 100\rangle$, can be used to check the validity of the model.

Acknowledgment

This work was partially supported by the NASA Marshall Space Flight Center, Huntsville, AL. The authors would like to thank Dr. Gregory R. Swanson at NASA MSFC for his extended help and support. The authors would also like to thank Dan Deluca, a fellow at Pratt & Whitney, East Hartford, CT, for his precious advice and active participation in the discussion.

References

[1] Cowles, B. A., 1996, "High Cycle Fatigue Failure in Aircraft Gas Turbines: An Industry Perspective," Int. J. Fract., **80**, pp. 147–163.
[2] Moroso, J., 1999, "Effect of Secondary Crystal Orientation on Fatigue Crack Growth in Single Crystal Nickel Turbine Blade Superalloys," MS thesis, University of Florida, Gainesville, FL.
[3] Deluca, D. P., and Annis, C., 1995, "Fatigue in Single Crystal Nickel Superalloys," Office of Naval Research, Department of the Navy, Technical Report No. FR23800.
[4] Swanson, G. R., and Arakere, N. K., 2000, "Effect of Crystal Orientation on Analysis of Single-Crystal, Nickel-Based Turbine Blade Superalloys," NASA, Marshall Space Flight Center, Technical Publication No. NASA/TP-2000-210074.
[5] Telesman, J., Fisher, D. N., and Holka, D., 1986, "Variables Controlling Fatigue Crack Growth of Short Crack," *Proceedings of the International Conference on Fatigue Corrosion Cracking Fracture Mechanics and Failure Analysis*, pp. 53–69.
[6] Ranjan, S., 2005, "Development of a Numerical Procedure for Mixed Mode K-Solutions and Fatigue Crack Growth in FCC Single Crystal Superalloys," Ph.D. thesis, University of Florida.
[7] Telesman, J., and Ghosn, L., 1989, "The Unusual Near-Threshold FCG Behavior of a Single Crystal Superalloy and the Resolved Shear Stress as the Crack Driving Force," Eng. Fract. Mech., **34**(5/6), pp. 1183–1196.
[8] Siddiqui, S., 2003, "Finite Element Analysis of Slip Systems in Single Crystal Superalloy Notched Specimens," MS thesis, University of Florida.
[9] Naik, R. A., Deluca, D. P., and Shah, D. M., 2004, "Critical Plane Fatigue Modeling and Characterization of Single Crystal Nickel Superalloys," Trans. ASME: J. Eng. Gas Turbines Power, **126**, pp. 391–400.
[10] Rice, J. R., 1968, "A Path Independent Integral and the Approximate Analysis of Strain Concentration by Notches and Cracks," ASME J. Appl. Mech., **35**, pp. 379–386.
[11] Sosa, H. A., and Eischen, J. W., 1986, "Computation of Stress Intensity Factors for Plate Bending Via a Path-Independent Integral," Eng. Fract. Mech., **25**(4), pp. 451–462.
[12] Parks, D. M., 1974, "A Stiffness Derivative Finite Element Technique for the Determination of Crack Tip Stress Intensity Factors," Int. J. Fract., **10**(4), pp. 487–502.
[13] Ishikava, H., 1980, "A Finite Element Analysis of Stress Intensity Factors for

Combined Tensile and Shear Loading by Only a Virtual Crack Extension," Int. J. Fract., **16**, pp. 243–246.
[14] Raju, I. S., 1987, "Calculation of Strain-Energy Release Rates With Higher Order and Singular Finite Elements," Eng. Fract. Mech., **28**(3), pp. 251–274.
[15] Atkinson, C., Smelser, R. E., and Sanchez, J., 1982, "Combined Mode Fracture Via the Cracked Brazilian Disk Test," Int. J. Fract., **18**(4), pp. 279–291.
[16] Shih, C. F., DeLorenzi, H. G., and German, M. D., 1976, "Crack Extension Modeling With Singular Quadratic Isoparametric Elements," Int. J. Fract., **12**(3), pp. 647–650.
[17] Awaji, H., and Sato, S., 1978, "Combined Mode Fracture Toughness Measurement by the Disk Test," ASME J. Eng. Mater. Technol., **100**, pp. 175–182.
[18] Su, R. K. L., and Sun, H. Y., 2003, "Numerical Solutions of Two-Dimensional Anisotropic Crack Problems," Int. J. Solids Struct., **40**, p. 4615–4635.
[19] Hwu, C., and Liang, Y., 2000, "Evaluation of Stress Concentration Factors and Stress Intensity Factors From Remote Boundary Data," Int. J. Solids Struct., **37**, pp. 5957–5972.
[20] Heppler, G., and Hansen, J. S., 1981, "Mixed Mode Fracture Analysis of Rectilinear Anisotropic Plates by High Order Finite Elements," Int. J. Numer. Methods Eng., **17**, pp. 445–464.
[21] Denda, M., and Marante, M. E., 2004, "Mixed Mode BEM Analysis of Multiple Curvilinear Cracks in the General Anisotropic Solids by the Crack Tip Singular Element," Int. J. Solids Struct., **41**, pp. 1473–1489.
[22] Mews, H., and Kuhn, G., 1988, "An Effective Numerical Stress Intensity Factor Calculation With No Crack Discretization," Int. J. Fract., **38**, pp. 61–76.
[23] Huang, H., and Kardomateas, G. A., 2001, "Stress Intensity Factors for a Mixed Mode Center Crack in an Anisotropic Strip," Int. J. Fract., **108**, pp. 367–381.
[24] Sun, Y.-Z., Yang, S.-S., and Wang, Y.-B., 2003, "A New Formulation of Boundary Element Method for Cracked Anisotropic Bodies Under Anti-Plane Shear," Comput. Methods Appl. Mech. Eng., **192**, pp. 2633–2648.
[25] Tweed, J., Melrose, G., and Kerr, G., 2000, "Stress Intensification Due to an Edge Crack in an Anisotropic Elastic Solid," Int. J. Fract., **106**, pp. 47–56.
[26] Pan, E., and Yuan, F. G., 2000, "Boundary Element Analysis of Three-Dimensional Cracks in Anisotropic Solids," Int. J. Numer. Methods Eng., **48**, pp. 211–237.
[27] Denda, M., 2001, "Mixed Mode I, II and III Analysis of Multiple Cracks in Plane Anisotropic Solids by the BEM: A Dislocation and Point Force Approach," Eng. Anal. Boundary Elem., **25**, pp. 267–278.
[28] Sih, G. C., Paris, P. C., and Irwin, G. R., 1965, "On Cracks in Rectilinearly Anisotropic Bodies," Int. J. Fract. Mech., **1**, pp. 189–203.
[29] Ingraffea, A., and Manu, C., 1980, "Stress-Intensity Factor Computation in Three Dimensions With Quarter-Point Elements," Int. J. Numer. Methods Eng., **15**, pp. 1427–1445.
[30] Lekhnitskii, S. G., 1963, *Theory of Elasticity of an Anisotropic Elastic Body*, Holden-Day, San Francisco.
[31] Saouma, V. E., and Sikiotis, E. S., 1986, "Stress Intensity Factors in Anisotropic Bodies Using Singular Isoparametric Elements," Eng. Fract. Mech., **25**(1), pp. 115–121.
[32] Deluca, D. P., private communication.
[33] Gell, M., and Liverant, G. R., 1968, "The Characteristics of Stage I Fatigue Fracture in a High Strength Nickel Alloy," Acta Metall., **16**(4), pp. 553–561.
[34] Gell, M., and Liverant, G. R., 1968, "The Fatigue of the Nickel-Base Superalloy, MAR-M200, in Single Crystal and Columnar-Grained Forms at Room Temperature," Trans. Metall. Soc. AIME, **242**, pp. 1869–1879.
[35] Duquette, D. J., Gell, M., and Piteo, J. W., 1970, "A Fractographic Study of Stage I Fatigue Cracking in a Nickel-Base Superalloy Single Crystal," Metall. Trans., **1**, pp. 3107–3115.
[36] Chen, O. Y., 1985, "Crystallographic Fatigue Crack Propagation in Single Crystal Nickel-Base Superalloy," Ph.D. thesis, University of Connecticut.
[37] Chan, K. S., Hack, J. E., and Liverant, G. R., 1987, "Fatigue Crack Growth in MAR-M200 Single Crystals," Metall. Trans. A, **18A**, pp. 581–591.
[38] Nageswararao, M., and Gerold, V., 1976, "Fatigue Crack Propagation in Stage I in an Aluminum-Zinc-Magnesium Alloy: General Characteristics," Metall. Trans. A, **7A**, pp. 1847–1855.
[39] McEvily, A. J., and Boettner, R. G., 1963, "On Fatigue Crack Propagation in F.C.C. Metals," Acta Metall., **11**(7), pp. 725–743.
[40] Chen, Q., and Liu, H. W., 1988, "Resolved Shear Stress Intensity Coefficient and Fatigue Crack Growth in Large Crystals," NASA, Syracuse University, Contractor Report No. CR-182137.
[41] Peach, M., and Koehler, J. S., 1950, "The Forces Exerted on Dislocations and the Stress Fields Produced by Them," Phys. Rev., **80**(3), pp. 436–439.
[42] Tada, H., Paris, P. C., and Irwin, G. R., 1985, *The Stress Analysis of Cracks Handbook*, Paris Productions, St. Louis.
[43] John, R., Deluca, D. P., Nicholas, T., and Porter, J., 1999, "Near Threshold Crack Growth Behavior of a Single Crystal Ni-Base Superalloy Subjected to Mixed Mode Loading," *Mixed-Mode Crack Behavior*, American Society for Testing Materials, Philadelphia, pp. 312–328.
[44] Suresh, S., 1998, *Fatigue of Materials*, 2nd ed., Cambridge University Press, Cambridge, England.